Acta Astronautica 177 (2020) 122–132

Contents lists available at ScienceDirect

Acta Astronautica

journal homepage: www.elsevier.com/locate/actaastro

Research paper

Maneuvering through solar wind using magnetic sails

Nikolaos Perakis *

Technical University of Munich, Boltzmannstr. 15, DE85748 Garching, Germany
Initiative for Interstellar Studies, Bone Mill, New Street, Charfield, GL12 8ES, United Kingdom

ARTICLE INFO

Keywords:
Magnetic sail
Interstellar plasma
Orbital plane change
Mission design
Trajectory optimization

ABSTRACT

The current study evaluates the performance of magnetic sails as a function of the incoming velocity and flow direction. A particle model is employed for the simulation of multiple angle-velocity combinations for the incoming ion flow, leading to a relationship between the drag force and the sail properties. Apart from the drag force, the model is able to predict lift and side forces on the sail. The importance of the non-axial forces is evident when designing plane-change maneuvers within the solar system. Using the solar wind and the correct magnetic sail pitch angle, a change in the inclination of the orbital plane can be achieved. A study is therefore presented using a single-coil magnetic sail starting in the ecliptic plane and employing a bang–bang control for the pitch angle. An increase of more than 30° in the orbital inclination is achieved within a 20 year time-frame.

1. Introduction

In an effort to maximize the available payload mass for a specific mission, innovative propellantless space propulsion techniques are very attractive for interplanetary and interstellar missions. Propellantless propulsion systems rely on the utilization of external power sources to produce thrust, instead of using on-board fuels and in this framework, the solar wind is one of the most promising candidates for available energy sources within the solar system. Apart from the concept of the electric sail [1] which consists of charged tethers that deflect the solar wind, the magnetic sail system is another propulsive device that has gained research interest in the past years.

The concept of using magnetic sails in order to take advantage of the interstellar plasma or the solar wind was first proposed by Zurbin and Andrews [2]. According to the concept of the magnetic sail, the magnetic field generated by a current-carrying coil can deflect incoming ions and therefore experiences a drag force. The main advantage is the absence of any propellant, meaning that the system is very efficient in terms of required mass.

The application of this component is very attractive for interstellar missions where it can be used to decelerate the probe to allow for an orbital insertion in the target star system without the need for additional propellant [3,4]. Combinations of magnetic and electric sails have also shown to be efficient for this purpose [5]. Apart from interstellar missions, the use in the design of interplanetary trajectories is also very interesting, as the solar wind can be utilized to change the semi-major axis of the orbit, allowing for missions to the outer or inner planets [2,6] and for the maintenance of circular, displaced, non-Keplerian orbits around the Sun [7].

For the simulation of the interaction of the plasma flow and the sail's magnetic field, several methods have been employed in the past. Magnetohydrodynamics approaches [8,9], particle in cell (PIC) methods [10,11] as well as hybrid methods [12,13] can be found in published literature. Scaling laws using particle simulations have also been derived for the axial magnetic sail configuration [14]. Experimental investigations of small-scale magnetic sails have been carried out serving as a proof of the working principle [15–17].

In the work presented here, a particle based method is implemented to describe the sail force dependence on the ion velocity for different configurations. The method is explained in detail in Section 2. The profiles for the drag, lift and side forces for different angle configurations are derived in Sections 3–5. The obtained dependencies are then used to design control laws for optimal interplanetary trajectories. Using a bang–bang control, a change in the orbital inclination of a heliocentric orbit is presented in Section 6.

2. Computational setup

In the nomenclature used throughout the paper, the reference coordinate system shown in Fig. 1 is used. The Z-axis is aligned with the incoming flow direction and is hence the direction at which the drag force is experienced. The X-axis is vertical to the flow direction and the Y-axis is chosen as to complete the orthogonal coordinate system. The

* Correspondence to: Technical University of Munich, Boltzmannstr. 15, DE85748 Garching, Germany.
E-mail address: nikolaos.perakis@tum.de.

https://doi.org/10.1016/j.actaastro.2020.07.029
Received 7 March 2020; Received in revised form 24 June 2020; Accepted 20 July 2020
Available online 24 July 2020

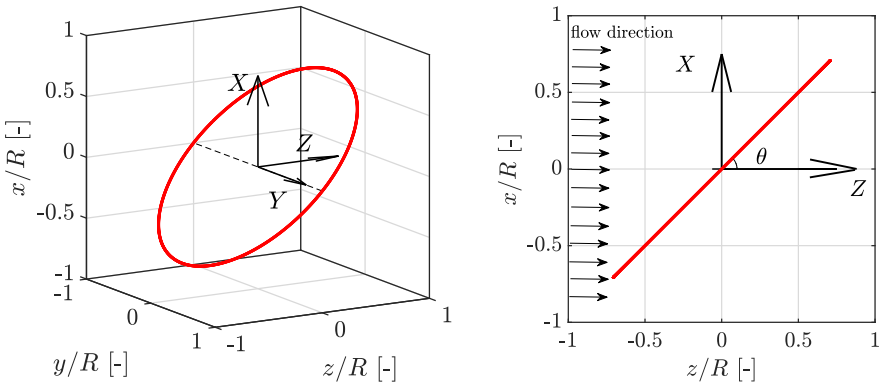

Fig. 1. Coordinate system and magnetic sail angle used in the present analysis. The red loop represents the magnetic sail.

magnetic sail's pitch angle is also defined as the angle θ in the right-subfigure of Fig. 1. This corresponds to the angle between the sail and the Z-axis, with $\theta = 90°$ representing the situation where the flow is aligned with the coil axis.

To simulate the interaction of the incoming ion flow with the magnetic field of the sail, a particle model is implemented. A series of particles is released from an inflow boundary, which interacts with the stationary magnetic field created by the magnetic sail.

The trajectory of each particle is described by the non-relativistic Lorentz force equation and the resulting ordinary differential equation (ODE) shown in Eq. (1) is integrated in time.

$$m_p \cdot \dot{\mathbf{v}} = q_p \mathbf{v} \times \mathbf{B} \tag{1}$$

where m_p and q_p represent the mass and electric charge of the ions respectively and $\mathbf{v}$ is their velocity.

In order to simulate the force imparted on the magnetic sail due to the incoming ion flow for each position within the domain $\mathbf{x}$, the magnetic field of the sail has been calculated using the Biot–Savart law:

$$\mathbf{B}(\mathbf{x}) = \frac{\mu_0 I}{4\pi} \int_L \frac{\mathrm{d}l' \times (\mathbf{x} - \mathbf{x}')}{|\mathbf{x} - \mathbf{x}'|^3} \tag{2}$$

where L represents the current carrying loop and I the current.

For a magnetic sail represented by a single loop of a coil, the resulting magnetic field strength is shown in Fig. 2. In this figure, the red arrow represents the direction of movement of the incoming ions. The coil is tilted with respect to the incoming velocity vector by an angle θ. Isolines of the magnetic field strength are also represented by solid black lines.

In the case where the angle θ is equal to 90°, i.e. when the coil axis is parallel to the incoming flow, the problem becomes axisymmetic. In all other configurations however, the problem has to be solved in a 3D domain.

To achieve that, the boundary inflow is meshed as shown in Fig. 3. For each inflow element with width dx and height dy, a particle is released. The trajectories of the individual exemplary particles are also plotted in the same figure after their interaction with the magnetic sail. Each of the particles imparts an infinitesimal force $\mathbf{dF}$ onto the sail which is given by:

$$\mathbf{dF} = -n_p \cdot m_p \cdot |\mathbf{v_0}| \cdot (\mathbf{v_F} - \mathbf{v_0}) \cdot dA \tag{3}$$

Note that this equation is valid since the Lorentz force is a conservative force, meaning that the magnitude of the particle velocity does not change during the interaction with the magnetic field, hence $v = |\mathbf{v_0}| = |\mathbf{v_F}|$. Note that the effect of the flow-induced electric field is neglected in this modeling approach. This results to an ion-orbit model which has been employed in the past for zero-order calculations of heat fluxes in fusion divertors [18] and for magnetic sail drag forces [14].

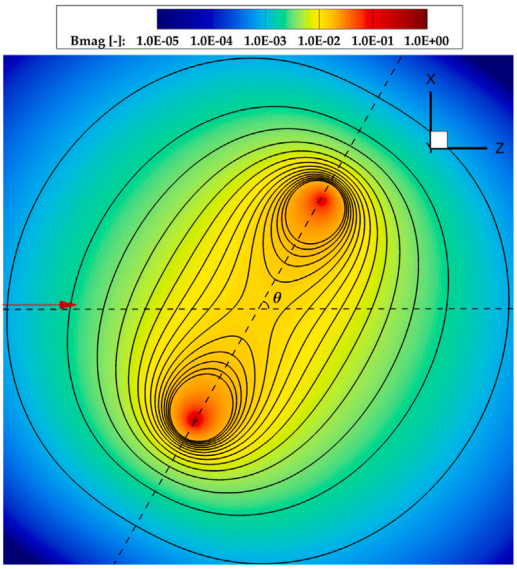

Fig. 2. Normalized magnetic field strength of a magnetic sail consisting of a single coil. The red arrow represents the incoming ion flow.

For each particle, the reflectivity factor S can be defined as the normalized inner product of the incoming and outgoing velocities:

$$S = \frac{\mathbf{v_0} \cdot \mathbf{v_F}}{|\mathbf{v_0}|^2} \tag{4}$$

A reflectivity factor of 1 would imply that the particles keep moving in the initial direction, i.e. unaffected by the magnetic field, whereas a value of −1 corresponds to a case where the particle's movement is reversed by 180°.

The total force on the sail is obtained by summing up all the contributions by the individual particles released into the domain:

$$\mathbf{F} = \int_A \mathbf{dF} \tag{5}$$

The position of the inlet plane is chosen so that the interaction of the magnetic field with the incoming flow is minimal at the boundary. The vertical and horizontal dimensions are also chosen in a way to ensure that the outer most particles are unaffected by the magnetic field strength. This is shown in Fig. 4, where the streamlines along the y-plane are shown along with the magnetic field lines. The coil is represented by the red line and is inclined by $\theta = 60°$ in the current configuration. One can recognize that the wake region behind the sail does not extend to the upper and lower bounds of the domain. This implies that the particles at the edge of the domain do not interact with

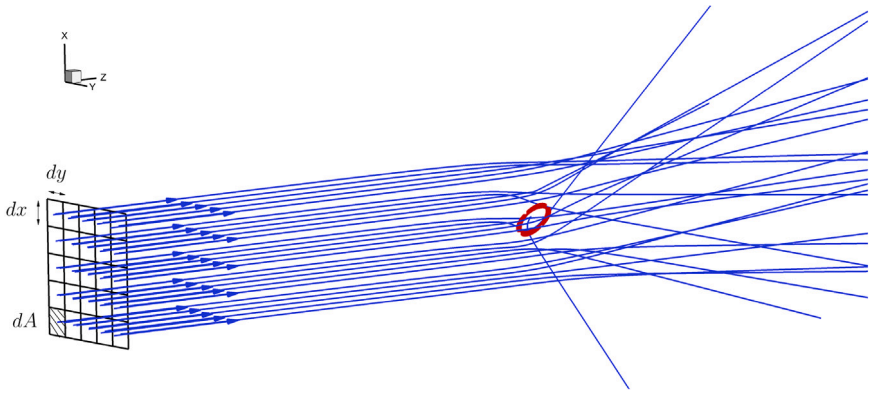

Fig. 3. Schematic overview of the inflow grid and interaction with the inclined magnetic sail.

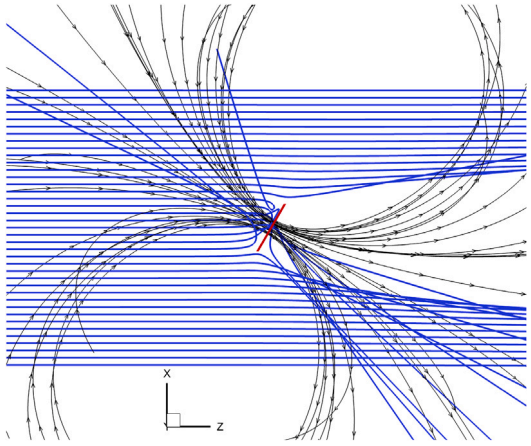

Fig. 4. Ion streamlines with superimposed magnetic field lines for an angle $\theta = 60°$. (For interpretation of the references to color in this figure legend, the reader is referred to the web version of this article.)

the sail and hence the size of the domain is adequate for this problem setup.

The resolution of the inlet grid has been examined to ensure that it does not influence the final results. A resolution of 800 × 800 particles has been chosen after a grid independence study. Note that the mesh is not uniform in x and y directions but rather is finer in the regions closer to the coil axis, as this is where the larger gradients are expected.

In the work of Gros [14], the effective area A is introduced, which is defined as in Eq. (6). This represents the area that a fully reflective sail would have.

$$A = \frac{F}{2m_p n_p \left|\mathbf{v_0}\right|^2} \tag{6}$$

In the current framework, we extend the notion of the effective area in all three space dimensions. We merely use this as tool to simplify the resulting expressions for the lift and side forces as shown in Section 5. Using this modeling approach, the effective area has three components, defined as:

$$\left[A_x, A_y, A_z\right]^T = \frac{1}{2m_p n_p \left|\mathbf{v_0}\right|^2} \cdot \left[F_x, F_y, F_z\right]^T \tag{7}$$

For the effective area in z direction (i.e. the one corresponding to the drag on the sail), the following expression can be utilized:

$$A_z = \int_0^\infty \int_0^\infty \frac{1 - S(x,y)}{2} dx dy \tag{8}$$

3. Drag for $\theta = 90°$

The majority of the previous studies investigating the performance of magnetic sails have focused on the configuration where the coil axis coincides with the incoming flow direction. This corresponds to the $\theta = 90°$ setup using the nomenclature introduced in this work. In this setup, the problem becomes axisymmetric and the use of a two-dimensional grid for the inlet boundary becomes obsolete. Instead, a 1D grid in radial direction is sufficient to describe the problem when dealing with particle methods. This is the approach also used by Gros [14].

In the current section, the dependence of the force on the incoming velocity of the ions is examined. The scaling relationship between the sail radius, the sail current and the axial velocity is already derived in [14]. For that reason, only the velocity of the ions is altered in the present section, for a constant sail size and current. To describe the velocity, the normalized velocity $\beta = v/c$ is used, where c is the speed of light.

In the left sub-figure of Fig. 5, the dependence of the reflectivity factor on the injection position of the particles and the particle velocity is shown. The injection position is described by the radial position x/R in this axisymmetric configuration, with $x = 0$ representing the axis of the sail. The right sub-figure illustrates the reflectivity profiles for three representative values of the velocity.

Starting from the lower β values one can observe that a large portion of the particles experience a large deflection due to the interaction with the magnetic sail. Specifically, for $\beta = 10^{-4}$ the reflectivity S is smaller than 1 for all particles injected at radial positions larger than $x/R = 0.15$, indicating a positive drag force. For positions with $x/R \leq 0.15$ the magnetic field lines are almost parallel to the incoming velocity vector leading to a negligible interaction.

For larger values for β it is evident that the interaction window starts shrinking. Specifically, for $\beta = 10^{-3}$ it extends from $x/R \approx 0.3$ up to $x/R \approx 6$ and for $\beta = 10^{-2}$ it only reaches up to $x/R \approx 2$. For further increased values of the velocity, the interaction window is negligible, leading to a complete absence of interaction between the particles and the magnetic sail. This can be inferred by the profile of reflectivity for $\beta = 10^{-1}$, which is constant and equal to 1 for all particle injection positions. The decreasing interaction magnitude for larger velocities can be explained by the smaller interaction time-scale that is available to them. Due to the higher speed, they spend less time in the presence of a sufficiently strong magnetic field and therefore interact minimally.

It can be hence deduced that the effective cross-sectional area of the sail decreases with increasing velocity. This finding is confirmed by Fig. 6, where the normalized area (in multiples of the physical sail cross-sectional area $\pi \cdot R^2$) is plotted. Despite the monotonically reducing area, the drag force is not experiencing the same behavior due to the quadratic contribution shown in Eq. (3). For that reason, an optimal velocity can be found for a given sail current and radius. The force results for a sail current $I = 10^5$ A, radius $R = 100$ m and

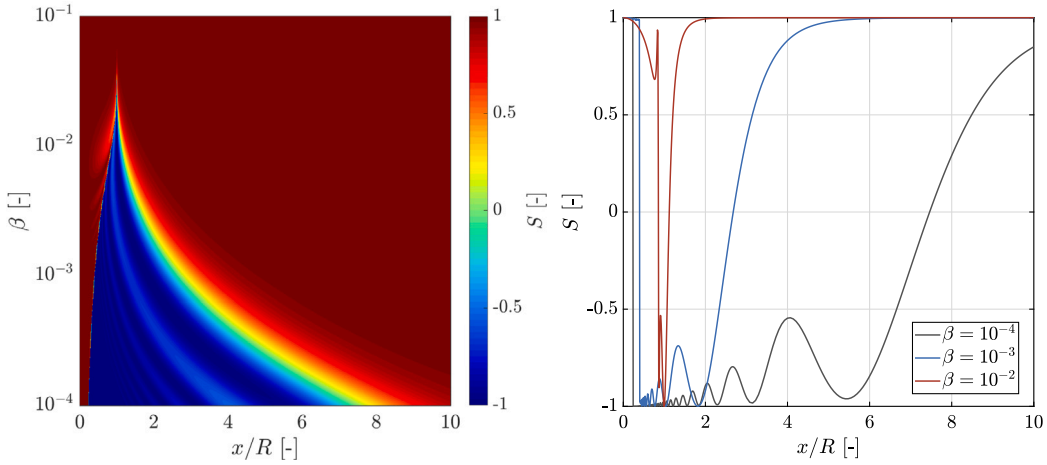

Fig. 5. Reflectivity factor as a function of the ion velocity and the injection position for a sail current $I = 10^5$ A and radius $R = 100$ m.

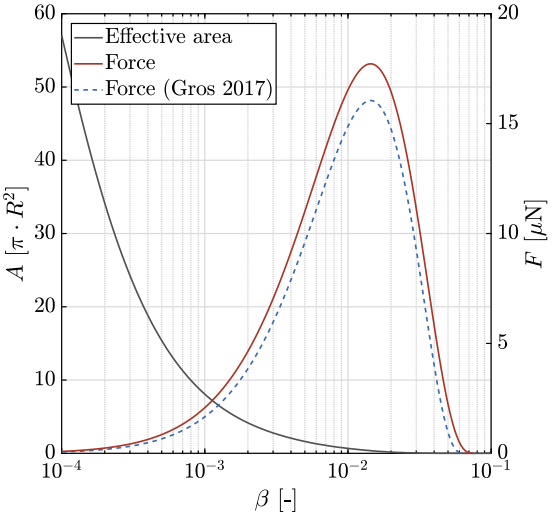

Fig. 6. Effective area and force as a function of velocity for the 90° (axial) sail configuration. A sail current of $I = 10^5$ A and sail radius $R = 100$ m is used.

an ion density $n_p = 0.05\,\mathrm{cm}^{-3}$ (corresponding to the expected values in the Local Bubble [19]) are also shown in Fig. 6. For the present configuration, the optimal is found for $\beta \approx 1.4 \cdot 10^{-2}$. The force profile is also compared to the results reported in Gros [14], demonstrating a very good agreement within 9%.

To describe the relationship between the velocity and the effective area, a scaling based on the work of Gros [14] is employed as shown in Eq. (9).

$$A_{z,90^\circ}(\beta) = \alpha_{z,90^\circ} \cdot \pi R^2 \cdot \left[\log\left(\frac{I}{\beta \cdot I_{z,c,90^\circ}}\right)\right]^{n_{z,90^\circ}} \tag{9}$$

The parameters in this equation have been determined by performing a least-squares fit with the numerical simulation results and are reported in Table 1. The results for the axial configuration strongly resemble the values found in [14], which are reported as $\alpha_{z,90^\circ} = 0.081$, $I_{z,c,90^\circ} = 1.55 \cdot 10^6$ and $n_{z,90^\circ} = 3$.

4. Dependency of drag on the angle of attack

Having established an approximation for the drag force in the axial configuration, the next step lies in examining how the force varies in relation to the sail angle of attack. For this reason, simulations have been carried out for multiple angle configurations ranging from $\theta = 0°$ up to $\theta = 90°$. The results for all further angles (in the range $90° \leq \theta \leq 360°$) can be inferred by a simple geometrical transformation using the $0° \leq \theta \leq 90°$ findings due to the symmetry of the problem.

Table 1
Fit parameters for the effective area formula.

Parameter	Value
$\alpha_{z,90^\circ}$	0.0599
$I_{z,c,90^\circ}$	$1.303 \cdot 10^6$
$n_{z,90^\circ}$	3.347
$\alpha_{z,0^\circ}$	$8.25 \cdot 10^{-7}$
$I_{z,c,0^\circ}$	$1.817 \cdot 10^4$
$n_{z,0^\circ}$	7.643
$\alpha_{y,1}$	$4.24 \cdot 10^{-4}$
$I_{y,c1}$	$1.336 \cdot 10^6$
$n_{y,\beta,1}$	6.128
$\alpha_{y,2}$	0.057
$I_{y,c2}$	$2.621 \cdot 10^6$
$n_{y,\beta,2}$	1.597
$n_{y,\theta}$	0.833

Examples of the ion streamlines for different angles of the sail can be seen in Fig. 7, where a coarse sample of all incoming ions is chosen for visualization purposes and the results along the $y = 0$ plane are shown.

In all four configurations a wake can be found downstream of the magnetic sail, similar to the flow around objects in typical fluid dynamic applications. However, some differences can be found when comparing the different angles of attack. First of all, the width of this wake appears to have its maximal value when the angle θ is equal to 90° and is reduced for lower attack angles. This implies that for smaller values of θ, the influence regime of the sail's magnetic field extends to a smaller range, meaning it reacts with less particles, at least along the y-plane. Nevertheless, this does not necessarily imply a larger drag for the $\theta = 90°$ setup. In fact, for the $\theta = 90°$ case, there are several particles that manage to go through the sail and exit the domain with little interaction with the magnetic field. As the angle is reduced, the number of unaffected particles drops. Therefore a more systematic way is required in order to evaluate the efficiency of the angle of attack in terms of achieved drag.

For that reason, the reflectivity factor as a function of the initial particle position is shown in Fig. 8. Three representative velocities ($\beta = 10^{-1}$, $\beta = 10^{-2}$, $\beta = 10^{-3}$) and four angles of attack ($\theta = 90°$, $\theta = 60°$, $\theta = 20°$, $\theta = 0°$) are chosen. In all of those plots, the effective area is proportional to the area in the figure which has reflectivity values less than 1, as elaborated in Eq. (8).

The first property which can be established for the velocity dependence is that the effective area appears to increase with smaller

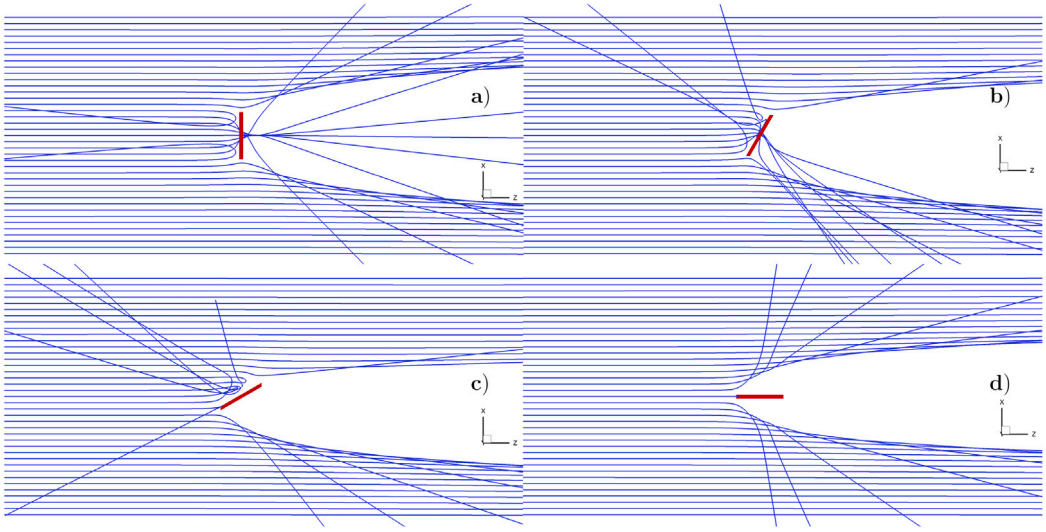

Fig. 7. Ion streamlines with $\beta = 10^{-2}$ along the $y = 0$ plane for different coil angles: (a) $\theta = 90°$, (b) $\theta = 60°$ (c) $\theta = 20°$, (d) $\theta = 0°$. A sail current $I = 10^5$ A and sail radius $R = 100$ m are used.

velocities for all different angles of attack. Although this fact was established already in Section 3 for the 90° case, now it is evident for other values of θ as well. Despite the increase in the effective area, the form of the contour-plots in Fig. 8 seems to remain mostly unaltered for different velocity values and is only scaled up, filling a larger part of the grid.

However, large discrepancies can be observed when comparing the different angles to each other. Starting from the 90° configuration, where the profiles are axisymmetric, decreasing the value of the angle leads to an increase in the complexity of the obtained reflectivity flow-fields. Specifically, for the smaller angles, interaction patterns with very small wavelengths can be observed. This implies a very high sensitivity of the reflectivity on the starting position of the ions, leading to a chaotic pattern.

Integrating the reflectivity over the entire domain and multiplying with the incoming ion impulse like in Eq. (3), leads to the total force of the different angles as a function of the velocity.

The resulting 2D curve as a function of β and θ as well as some line plots for representative β values are shown in Fig. 9. In the left sub-figure, the markers represent the simulation points and the solid surface the resulting numerical fit, which will be explained in this section. It is evident from the figure, that the force on the sail is maximal for the 0° configuration, independent from the incoming velocity. This is an important finding, as it implies that the axial configuration is less efficient in the velocity range examined here. Moreover, the form of the force–velocity profile seems to change for different angles of attack. Whereas the profile for 90° has its maximal value for approximately $\beta = 1.5 \cdot 10^{-2}$ as already seen in Fig. 6, the 0° configuration has no local maximum and is a monotonically increasing function within the examined velocity range. By investigating the other angle values as well, it appears that the maximum force is achieved for higher velocities than for the axial sail configuration, as the angle is decreased. It is therefore expected that the 90° force will also reach a maximum which however corresponds to a value $\beta > 0.1$. As relativistic effects become relevant in those speeds, no simulations have been carried out to confirm this assumption.

Nevertheless, similar to the analysis performed in Section 3, a numerical fit of the effective area in the 0° configuration has also been performed, using the same scaling law as in Eq. (9):

$$A_{z,0°}(\beta) = \alpha_{z,0°} \cdot \pi R^2 \cdot \left[\log\left(\frac{I}{\beta \cdot I_{z,c,0°}}\right)\right]^{n_{z,0°}} \tag{10}$$

The fit parameters can be found in Table 1. For the description of the force dependence on both the angle and the velocity, a blending of the force for the two extreme configurations (90° and 0°) using the hyperbolic tangent function was found to be suitable. This is described in Eq. (11). The chosen fit is shown with the 2D curve in Fig. 9 and exhibits a maximal deviation of 9% from the simulated values.

$$F_z(\beta,\theta) = F_{z,90°}(\beta) + 0.5 \cdot \left[\tanh\left(2.5 \cdot \left(\frac{\pi}{4} - \theta\right)\right) + 1\right] + \left(F_{z,0°}(\beta) - F_{z,90°}(\beta)\right) \tag{11}$$

5. Lift and side forces

Apart from changing the dependence of the drag force on the velocity, an angle of attack different that 90° also introduces force components along the axes perpendicular to the incoming ion velocity. This will be referred to as "lift forces" (along the x-axis based on the coordinate system in Fig. 3) and "side forces" along the y-axis.

An example for the side force experienced by the sail can be seen in Fig. 10, where the streamlines of the particles injected at $x = 0$ are drawn. An asymmetrical deflection of their trajectories can be inferred from the figure with a tendency towards the positive y-axis. In this particular case, the deviation in positive and negative y-axis appears to be unbalanced, leading to a net side force on the sail. The side force has also been explored in previous studies [12].

To understand the origin of the side force, one can examine the magnetic field lines in Fig. 4, where the sail angle θ is lower than 90°. Both for the upper ($x > 0$) and lower half ($x < 0$), the magnetic field lines passing through the coil (close to its axis), point in the same direction along the vertical, i.e. downwards in x-direction. Hence according to the Lorentz force, both in the upper and lower halves of the domain, the ions (which move in positive z direction) interacting with the field will experience a force along the positive y-axis. Therefore, the side forces in the upper and lower half do not cancel out but get added.

A typical profile of the drag, lift and side forces as a function of the angle of attack is shown in Fig. 11. The velocity chosen for this plot corresponds to $\beta = 10^{-2}$ but the same qualitative trend can be seen for all velocity values without loss of generality. The absolute force values correspond to a sail current $I = 10^5$ A, radius $R = 100$ m and an ion density $n_p = 0.05\,\mathrm{cm}^{-3}$. Following the convention of the chosen coordinate system, F_z is the drag force, F_x the lift and F_y the side force.

As expected, both the lift and side force are zero for the 90° configuration. For the 0° setup, the lift disappears but there is still a non-negligible side force. The reason for the non-disappearing side force is that for the flat sail ($\theta = 0°$), both the ions flowing over the sail as well as the ones flowing under it, experience a force in the same

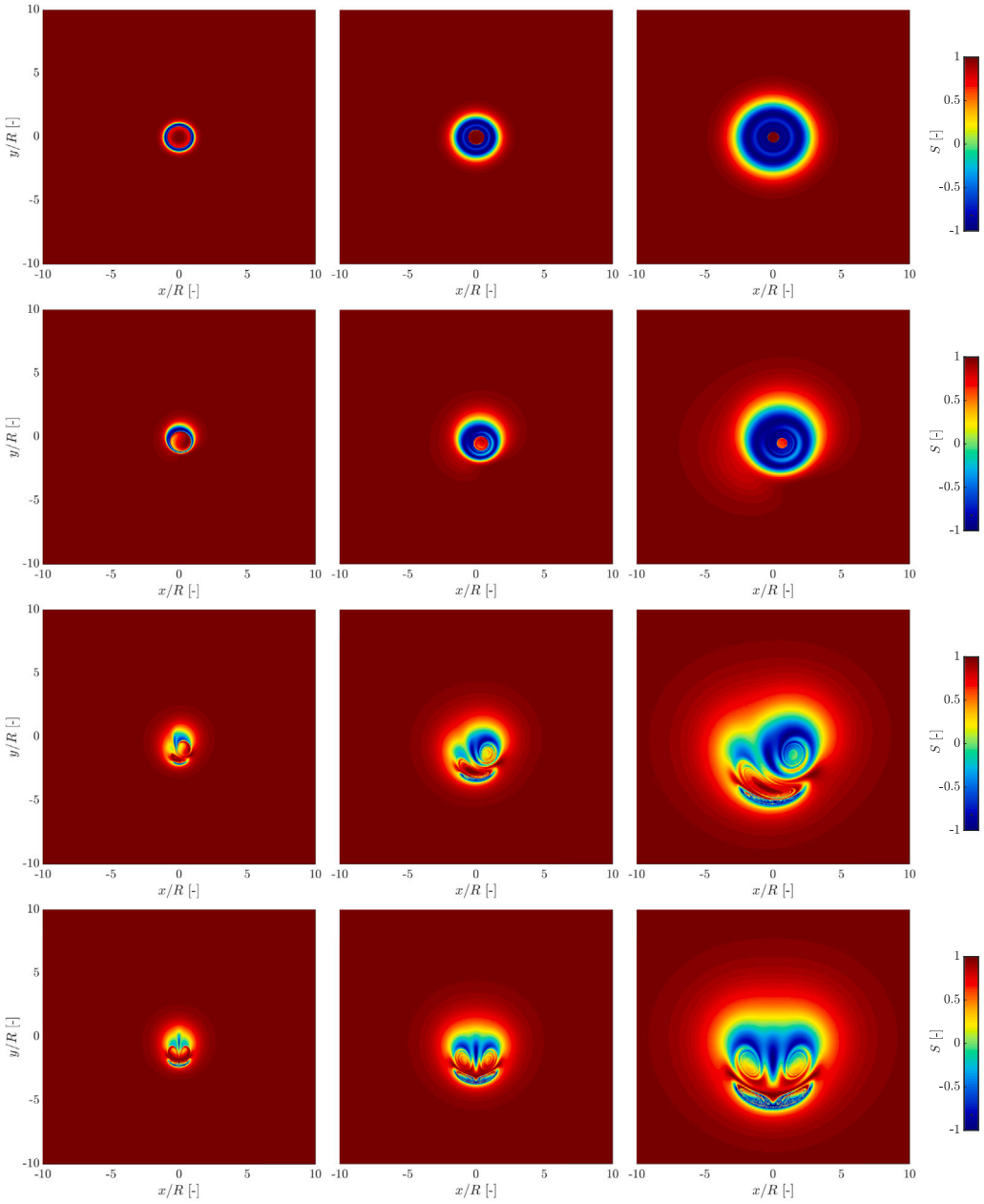

Fig. 8. S reflectivity factor for different velocities (from left to right: $\beta = 10^{-1}$, $\beta = 10^{-2}$, $\beta = 10^{-3}$) and different angles (from top to bottom: $\theta = 90°$, $\theta = 60°$, $\theta = 20°$, $\theta = 0°$). A sail current $I = 10^5$ A and sail radius $R = 100$ m are used.

direction and hence no canceling of the net contribution can occur. The lift on the other hand vanishes as the setup is symmetric with respect to the x-axis.

The lift force appears to be negative for all other angles between the two extreme configurations. The sign of the force is not that important as a change of the current direction or a flip of the sail by 180° would produce a positive value. For that reason only the magnitude of the force will be discussed. This appears to steadily increase until 30° and then continuously drop back down to zero for $\theta = 90°$. The side force on the other hand seems to have a plateau value for angles between 0° and 40°. Only for larger values does it start dropping further towards 0. In the same figure, the tangent hyperbolic nature of the drag force is visible, as already established in Section 3. The profiles for the drag and the lift forces are in qualitative agreement with the work of Kajimura et al. [12].

The combined dependence of the lift and side forces on the velocity and angle is illustrated in Fig. 12. It can be seen that in contrast to the drag force shown in Fig. 9, the lift and side force are monotonically increasing with the velocity, independent from the magnetic sail angle.

Due to the relatively complex form of the lift force curve, no numerical fit has been performed but rather a Kriging meta-model has been used [20]. The side force on the other hand can be described with satisfying accuracy based on Eqs. (12)–(13). The corresponding parameters are listed in Table 1.

$$A_y(\beta,\theta) = A_y(\beta)\cdot[\cos(\theta)]^{n_{y,\theta}} \tag{12}$$

$$A_y(\beta) = \pi R^2 \cdot \left[\alpha_{y,1}\cdot\left(\log\left(\frac{I}{\beta\cdot I_{y,c1}}\right)\right)^{n_{y,\beta1}} + \alpha_{y,2}\cdot\left(\log\left(\frac{I}{\beta\cdot I_{y,c2}}\right)\right)^{n_{y,\beta2}}\right] \tag{13}$$

6. Orbital plane change using magnetic sail

Several studies have been performed investigating the suitability of magnetic sails for maneuvering within the solar system. In contrast to

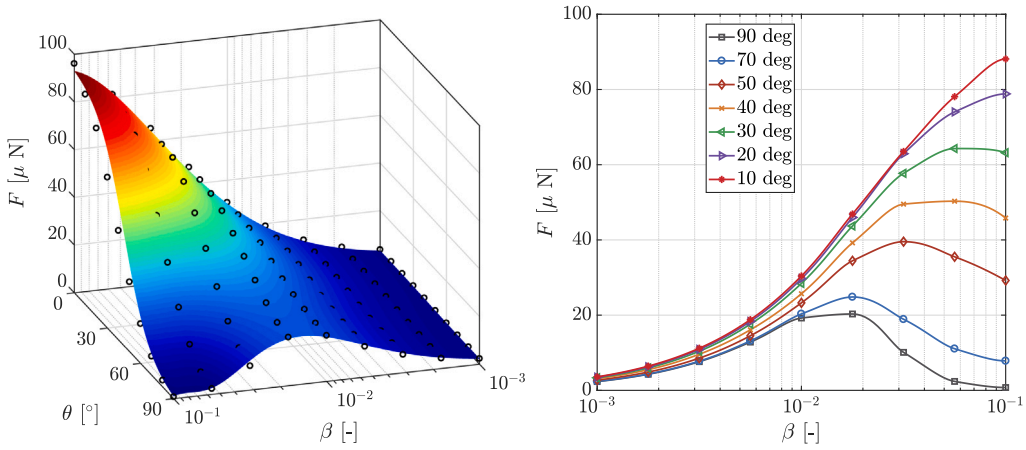

Fig. 9. Drag force as a function of the angle of attack and the incoming ion velocity. A sail current $I = 10^5$ A and sail radius $R = 100$ m are used.

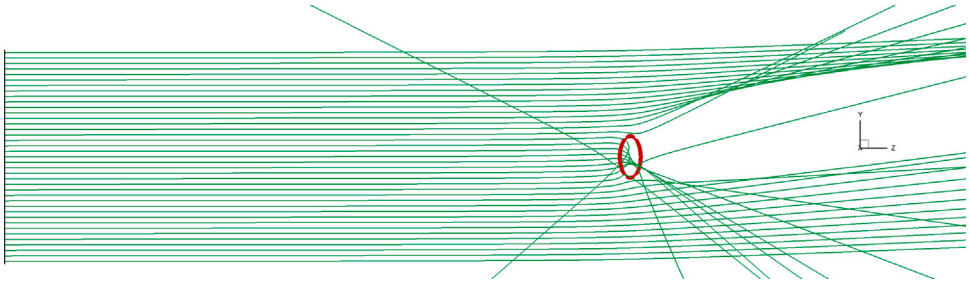

Fig. 10. Streamlines of ions with starting positions along the $x = 0$ line for $\beta = 10^{-2}$ and $\theta = 60°$. A sail current $I = 10^5$ A and sail radius $R = 100$ m are used.

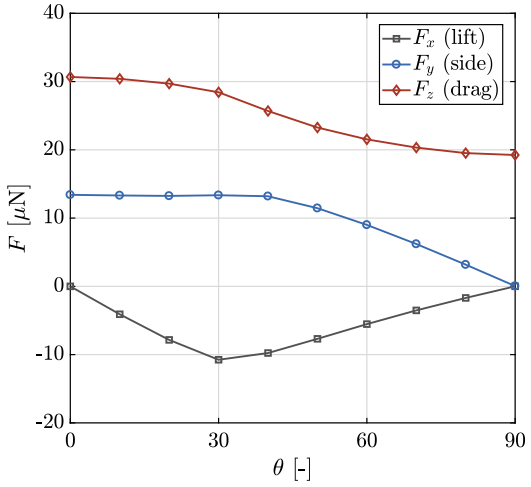

Fig. 11. Drag, lift and side force as a function of the magnetic sail angle for $\beta = 10^{-2}$. A sail current $I = 10^5$ A and sail radius $R = 100$ m are used.

interstellar missions, where the magnetic sail can be employed as a propellantless propulsion system which brakes the spacecraft against the interstellar medium, in interplanetary missions the driver for the magnetic sail force is the solar wind. In the present section, the performance of the magnetic sail within the magnetic wind environment is assessed for different mission scenarios based on the force curves derived in Sections 3–5.

For all simulations presented here, the Gaussian form of the Kepler elements variation is used [21]. According to this model, the variation of the orbital elements $a, e, i, \Omega, \omega, M_0$ is described as a function of the perturbing acceleration vector $\mathbf{a_p}$:

$$\mathbf{a_p} = \left[a_r, a_s, a_w\right]^T \tag{14}$$

The three components of the perturbation acceleration are aligned with three principal axes (black color) shown in Fig. 13. "R" represents the radial direction, "S" the local horizon and "W" the normal to the orbital plane.

As a perturbing acceleration, only the solar wind effect on the magnetic sail is accounted for. Third body contributions like Jupiter's and Saturn's gravitational fields are ignored for the present analysis due to their non-secular but rather periodic nature and in order to isolate the effect of the magnetic sail. In Fig. 13, the already introduced coordinate system of the magnetic sail is illustrated in red color. It is evident that the drag and lift forces are aligned with the radial and normal directions respectively, whereas the side force is showing in the opposite direction of the local horizon. Therefore, the correlation between the perturbing acceleration and the magnetic sail forces experiences the following rule:

$$\left[a_r, a_s, a_w\right]^T = \frac{1}{m_{tot}} \cdot \left[F_z, -F_y, F_x\right]^T \tag{15}$$

where m_{tot} stands for the total mass of the spacecraft with the magnetic sail system.

The solar wind environment is modeled using two parameters, the solar wind particle density $n_{p,SW}$ and the solar wind velocity v_{SW}. The values for the ecliptic and polar solar wind velocity have been taken from McComas et al. [22], and are in the range $v_{SW} = 400$–750 km/s, corresponding to $\beta = 1.3 \cdot 10^{-3} - 2.5 \cdot 10^{-3}$. For the number density $n_{p,SW}$, a quadratic law is used according to:

$$n_{p,SW}(r) = n_{p,AU} \frac{r_{AU}^2}{r^2} \tag{16}$$

with a conservative estimate $n_{p,AU} = 5\,\mathrm{cm}^{-3}$ [2].

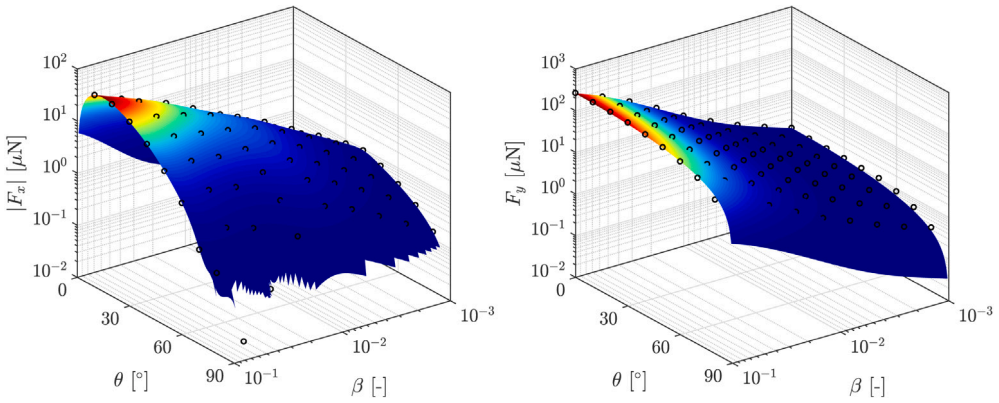

Fig. 12. Lift (F_x) and side (F_y) forces as a function of velocity and angle. A sail current $I = 10^5$ A and sail radius $R = 100$ m are used.

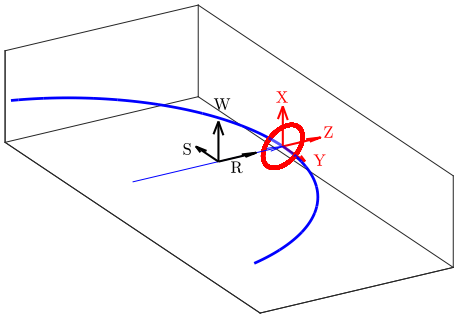

Fig. 13. Coordinate systems used in the orbital analysis. (For interpretation of the references to color in this figure legend, the reader is referred to the web version of this article.)

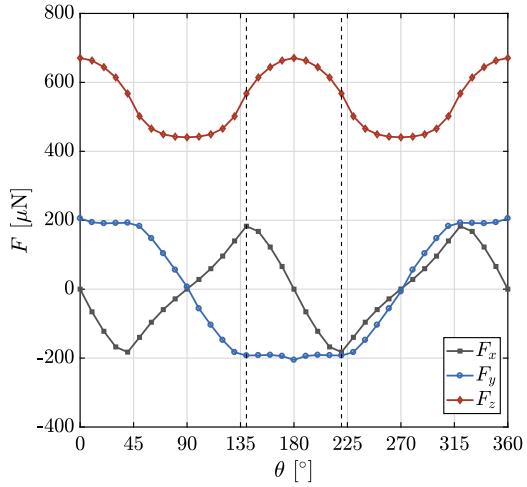

Fig. 14. Magnetic sail forces in the solar wind for a sail with $R = 350$ m and $I = 10^4$ A at a distance of 1 AU from the sun as a function of the sail angle.

For the sail design, a radius $R = 350$ m and a current $I = 10^4$ A is utilized. The resulting drag, lift and side forces as a function of the magnetic sail angle in the ecliptic plane (using $\beta_{SW} = 1.67 \cdot 10^{-3}$) at a distance of 1 AU from the sun are plotted in Fig. 14. The results for angles larger than 90° are obtained after symmetry considerations of the results shown in Section 5.

For all three scenarios presented here, the same magnetic sail configuration, spacecraft mass and initial orbit are used. A spacecraft mass (excluding the magnetic sail system) of 450 kg is assumed, similar to the mass of the New Horizons probe [23]. In order to estimate the mass of the current carrying loop, a maximal current density $j_{max} = 10^6$ A/cm^{-2} is used [24,25] together with a density $\rho = 9000$ kg/m^3 which is a conservative estimate for superconductors based on copper oxide (CuO) and YBCO. For a sail radius equal to $R = 350$ m, this results to a coil mass of 40 kg. Additional tethers, attitude control system for the sail, shielding mass and power system have been estimated with a conservative estimate of 275% of the coil mass. The masses of each individual subsystem (relative to the coil mass) are reported as follows and are based on the work of Raible [26]:

1. Deployment spool mass: 30% - 12 kg
2. Tethers mass: 70% - 28 kg
3. Tether shielding mass: 30% - 12 kg
4. Sail shielding mass (based on the Benedikt method [27]): 85% - 34 kg
5. Additional power system: 60% - 24 kg

No active cooling system is included as a high-temperature superconducting material is assumed. With those assumptions, the total mass of the magnetic sail system is 150 kg and the total mass of the probe reaches m_{tot}=600 kg. The ratio of sail to total mass based on these estimates amounts to 25%, which is within the range of values reported by Zubrin et al. [2] (13%), by Häfner [3] (36%) and Perakis et al. [4] (30%).

With this setup, three distinct scenarios are simulated. In all three missions, the starting orbit corresponds to $a_0 = 1$ AU, $e_0 = 0.0167$, $i_0 = 23.44°$ with a characteristic energy relative to the earth $C_3 = 0$ km^2/s^2. The first scenario corresponds to an increase of the semi-major axis of the probe, representing a mission to the outer planets. In the second scenario, a mission to the inner planets (in this case Mercury) is simulated. Finally, a trajectory with a combined increase of both the semi-major axis and the inclination is calculated.

The choice of the optimal magnetic sail pitch angle for the first two scenarios can be derived by looking at the Gauss form of the Lagrange planetary equations and specifically the equation for semi-major axis, as shown in Eq. (17).

$$\frac{da}{dt} = \frac{2e\sin(\nu)}{n\sqrt{1-e^2}} \cdot a_r + \frac{2a\sqrt{1-e^2}}{nr} \cdot a_s \tag{17}$$

In the current notation, ν is the true anomaly, a the semi-major axis, e the eccentricity, n the mean motion and r the orbital distance. Both a radial outwards acceleration (a_r) and an acceleration along the local horizon (a_s) have a positive effect on the increase of the orbit's semi-major axis, with the acceleration along the S-axis having a much larger influence. Therefore for an increase of the semi-major axis (mission to the outer planets), the most effective sail configuration should provide $F_s > 0$ and hence $F_y < 0$ based on Eq. (15), whereas for a mission to the inner planets $F_y > 0$ is optimal. In the first two scenarios, the additional constraint of constant inclination is introduced. In order to

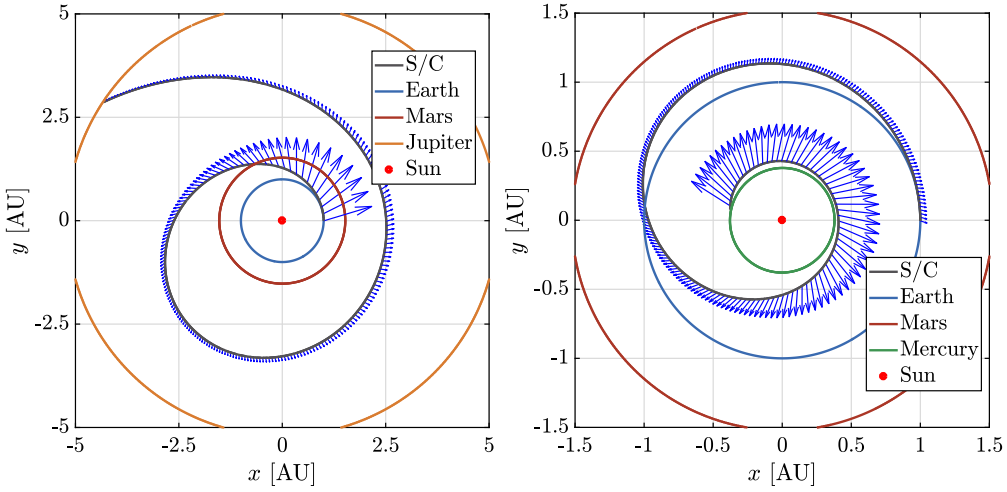

Fig. 15. Spiral outwards (left) and inwards (right) trajectories for $\theta = 180°$ and $\theta = 0°$. A sail with $R = 350\,\text{m}$ and $I = 10^4\,\text{A}$ is chosen, with a total spacecraft mass of 600 kg.

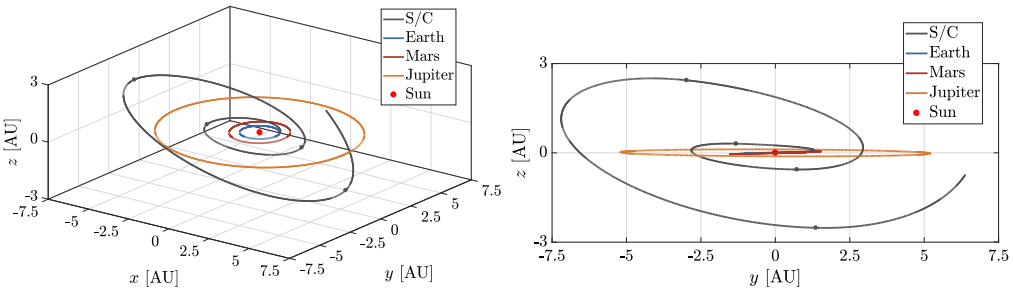

Fig. 16. Trajectory of the spacecraft during the plane change maneuver. A sail with $R = 350\,\text{m}$ and $I = 10^4\,\text{A}$ is chosen, with a total spacecraft mass of 600 kg. This corresponds to the first 20 years of the mission.

achieve that, the off-plane acceleration component (lift force) has to be zero, as shown in the Lagrange equation for the inclination:

$$\frac{di}{dt} = \frac{r\cos(\omega + \nu)}{na^2\sqrt{1-e^2}} \cdot a_w \tag{18}$$

where ω stands for the argument of periapsis. With those constraints and with the established results shown in Fig. 14, a unique solution for the optimal open-loop control can be found: for the mission towards the outer planets, $\theta = 180°$ is chosen and for missions towards the inner planets, $\theta = 0°$ is applied.

The resulting orbit for those two scenarios is illustrated in Fig. 15. Note that those trajectories are not optimal trajectories but rather example transfers, demonstrating the capability of the magnetic sail as a propulsion system using a constant sail angle. In both cases, the blue arrows represent the magnetic sail forces and are scaled with the relative magnitude of the force for each configuration. As expected, due to the modeling choices for the solar wind density, the force magnitude drops quadratically with increasing distance from the sun. Due to this fact, the inwards spiral is achieved very efficiently, with a total mission duration of 1 year, whereas for the outward mission approximately 6.5 years have to elapse.

The application of magnetic sails for the increase or decrease of the semi-major axis in order to facilitate interplanetary missions has been the subject of several studies in the past [6]. However little research has been performed on analyzing a potential off-plane maneuver using magnetic sails. The derivation of the lift and side forces in the present work allows for the design of such an off-plane maneuver. Orbital inclination changes using impulsive maneuvers typically occur at the orbital nodes and require large amounts of propellant. This is also the reason why most interplanetary missions requiring a plane-change rely

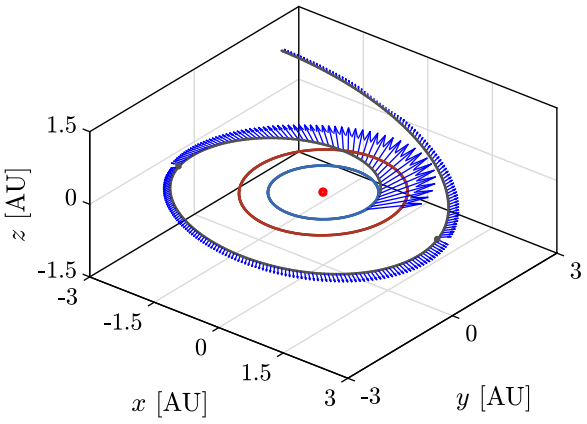

Fig. 17. Trajectory of the probe for the plane change mission with corresponding acceleration vectors. A sail with $R = 350\,\text{m}$ and $I = 10^4\,\text{A}$ is chosen, with a total spacecraft mass of 600 kg. This corresponds to the first 6 years of the mission.

on gravitational assist, which however significantly increases the mission duration. Having a propellant-less alternative for those expensive maneuvers can be very useful, especially regarding potential missions to discovered interstellar asteroids which typically have trajectories that are not aligned with the ecliptic plane [28,29].

Using the insights given by Eq. (18), in order to achieve a monotonically increasing inclination over time, the term $\cos(\omega+\nu)\cdot a_w$ has to be positive. As the sign of the $\cos(\omega + \nu)$ factor changes at the perihelion and aphelion (for $\omega = 0°$), the optimal control requires a change in the pitch angle over time. Specifically, in the first half of the orbit where

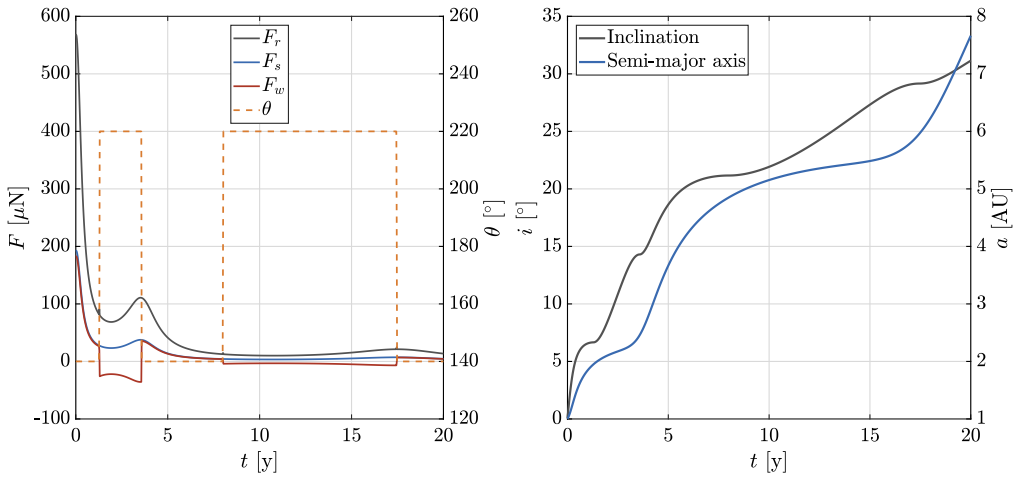

Fig. 18. Magnetic sail forces (left) as well as semi-major axis and inclination (right) as a function of the mission time. A sail with $R = 350\,\text{m}$ and $I = 10^4\,\text{A}$ is chosen, with a total spacecraft mass of 600 kg.

$90° < \omega + \nu < 270°$, a negative acceleration a_w is required, whereas for the second half of the orbit, a positive acceleration is needed. This coincides with the findings reported by Rugiero et al. [30] for the design of low-thrust trajectories. Therefore, in order to maximize both the inclination increase and the semi-major increase at the same time, the following values for θ are chosen:

$$\begin{cases} \theta = 220° & \cos(\omega + \nu) < 0 \\ \theta = 140° & \cos(\omega + \nu) > 0 \end{cases}$$

The optimal control values are also indicated in Fig. 14 with the vertical dashed lines. Using this bang–bang open loop control, the trajectory of the probe is simulated within a time-frame of 20 years. Note that those trajectories are not optimal trajectories but rather example transfers, demonstrating the capability of the magnetic sail as a propulsion system. The resulting orbit is shown in Fig. 16. The black dots indicate the locations where the change in the orientation of the magnetic sail occurs. In the right sub-figure of Fig. 16, a side-view of the orbital plane is shown, clearly demonstrating the increase in the orbital inclination.

The orientation of the resulting force generated by the interaction between the solar wind and the sail can be found in Fig. 17 for the same trajectory. Here, only the first 6 years of the orbit are shown for visualization purposes. A fast flip in the direction of the acceleration vector can be observed in the two instances where the spacecraft passes through the location corresponding to $\cos(\omega+\nu) = 0$, which is the result of the bang–bang control loop.

A clear view of the magnetic sail angle as well as the resulting forces are shown in the left sub-figure of Fig. 18. As expected, the radial force is always larger than zero, since there is no configuration producing a negative drag. Moreover, since a positive force along the local horizon has been enforced, F_s also remains larger than zero for the entire trajectory. On the other hand, the only force being affected by the active control is the off-plane component F_w which alternates between negative and positive values depending on the position along the orbital track. All three components show a decrease in magnitude over time, which is explained by the increasing distance from the sun.

The resulting profiles for the orbital elements of interest are shown in the right sub-figure of Fig. 18. For the semi-major axis, a steady increase over time is visible, stemming from the continuous acceleration along the local horizon and the radial direction. For the inclination, additionally to the increasing value, the locations where the change in control angle occurs are also easy to spot. Specifically, one notices the locations where the profile becomes flatter and where its time derivative approaches zero; those locations correspond to the situation where $\cos(\omega + \nu) = 0$.

7. Conclusion

In the present work, the interaction between incoming ions and a magnetic sail consisting of a single current carrying loop has been investigated. Specifically, a three-dimensional particle simulation using the Lorentz force and the Biot–Savart law for simulation of the trajectory of individual ions has been utilized.

By simulating various starting initial conditions of the incoming ions, a relationship between the drag force and the velocity is obtained. The scaling of this force with the sail current and size is in agreement with previous studies serving as a validation of the model. Apart from the axial configuration, where the sail's axis and the incoming velocity vector coincide, various angles for the sail's angle of attack have been simulated. This resulted in a complex dependence of the drag force on the sail's relative angle and speed with respect to the incoming flow.

Furthermore, the quantification of the lift and side forces has been also been performed, showing that they are non-negligible for all configurations where $\theta \neq 90°$. An accurate description of those values is very important in the design stage of a potential interplanetary mission. The reason is that the lift component of the thrust can allow for an acceleration vertical to the orbital plane, hence leading to a change in inclination.

Using this finding, the trajectory of a probe equipped with a magnetic sail has been carried out, demonstrating an efficient change both in the semi-major axis and in inclination. This method of acceleration could replace or assist expensive impulsive maneuvers for plane change or time-consuming gravity assists.

An extension of the current investigation to include an analysis of the thrust components due to a variation of the yaw angle is also necessary to completely describe the efficiency of a magnetic sail. Such a study is planned and would introduce additional degrees of freedom when designing interplanetary and interstellar missions, as it would allow more complex thrust vector configurations and a more detailed control of the desired trajectory.

Nevertheless, the simplicity of the employed ion model for the force calculation has to be mentioned. Since the electric field has been neglected in this study and the simulation is merely an ion orbit calculation, the resulting forces can be assumed as a zeroth-order approximation. Studies using particle-in-cell code are planned in order to quantify the effect of the electrons and the induced electric fields on the thrust vector.

Declaration of competing interest

The authors declare that they have no known competing financial interests or personal relationships that could have appeared to influence the work reported in this paper.

References

[1] P. Janhunen, Electric sail for spacecraft propulsion, J. Propul. Power 20 (4) (2004) 763–764, http://dx.doi.org/10.2514/1.8580.

[2] R.M. Zubrin, D.G. Andrews, Magnetic sails and interplanetary travel, J. Spacecr. Rockets 28 (2) (1991) 197–203, http://dx.doi.org/10.2514/3.26230.

[3] T. Häfner, M. Kushwaha, O. Celik, F. Bellizzi, Project Dragonfly: Sail to the stars, Acta Astronaut. 154 (2019) 311–319, http://dx.doi.org/10.1016/j.actaastro.2018.05.018.

[4] N. Perakis, L.E. Schrenk, J. Gutsmiedl, A. Koop, M.J. Losekamm, Project Dragonfly: A feasibility study of interstellar travel using laser-powered light sail propulsion, Acta Astronaut. 129 (2016) 316–324, http://dx.doi.org/10.1016/j.actaastro.2016.09.030.

[5] N. Perakis, A.M. Hein, Combining magnetic and electric sails for interstellar deceleration, Acta Astronaut. 128 (2016) 13–20, http://dx.doi.org/10.1016/j.actaastro.2016.07.005.

[6] A.A. Quarta, G. Mengali, G. Aliasi, Optimal control laws for heliocentric transfers with a magnetic sail, Acta Astronaut. 89 (2013) 216–225, http://dx.doi.org/10.1016/j.actaastro.2013.04.018.

[7] M. Bassetto, A.A. Quarta, G. Mengali, Magnetic sail-based displaced non-keplerian orbits, Aerosp. Sci. Technol. 92 (2019) 363–372, http://dx.doi.org/10.1016/j.ast.2019.06.018.

[8] H. Nishida, H. Ogawa, I. Funaki, K. Fujita, H. Yamakawa, Y. Inatani, Verification of momentum transfer process on magnetic sail using MHD model, in: 41st AIAA/ASME/SAE/ASEE Joint Propulsion Conference & Exhibit, AIAA Paper 2005–4463, 2005, http://dx.doi.org/10.2514/6.2005-4463.

[9] H. Nishida, H. Ogawa, I. Funaki, K. Fujita, H. Yamakawa, Y. Nakayama, Two-dimensional magnetohydrodynamic simulation of a magnetic sail, J. Spacecr. Rockets 43 (3) (2006) 667–672, http://dx.doi.org/10.2514/1.15717.

[10] K. Fujita, Particle simulation of moderately-sized magnetic sails, J. Space Technol. Sci. 20 (2) (2004) 2_26–2_31, http://dx.doi.org/10.11230/jsts.20.2-26.

[11] Y. Ashida, I. Funaki, H. Yamakawa, Y. Kajimura, H. Kojima, Thrust evaluation of a magnetic sail by flux-tube model, J. Propul. Power 28 (3) (2012) 642–651, http://dx.doi.org/10.2514/1.B34332.

[12] Y. Kajimura, I. Funaki, M. Matsumoto, I. Shinohara, H. Usui, H. Yamakawa, Thrust and attitude evaluation of magnetic sail by three-dimensional hybrid particle-in-cell code, J. Propul. Power 28 (3) (2012) 652–663, http://dx.doi.org/10.2514/1.B34334.

[13] I. Funaki, Y. Nakayama, Sail propulsion using the solar wind, J. Space Technol. Sci. 20 (2) (2004) 2_1–2_16, http://dx.doi.org/10.11230/jsts.20.2_26.

[14] C. Gros, Universal scaling relation for magnetic sails: momentum braking in the limit of dilute interstellar media, J. Phys. Commun. 1 (4) (2017) 045007, http://dx.doi.org/10.1088/2399-6528.

[15] I. Funaki, H. Kojima, H. Yamakawa, Y. Nakayama, Y. Shimizu, Laboratory experiment of plasma flow around magnetic sail, in: High Energy Density Laboratory Astrophysics, Springer, 2006, pp. 63–68, http://dx.doi.org/10.1007/978-1-4020-6055-7-12.

[16] K. Ueno, I. Funaki, T. Kimura, H. Horisawa, H. Yamakawa, Thrust measurement of a pure magnetic sail using parallelogram-pendulum method, J. Propul. Power 25 (2) (2009) 536–539, http://dx.doi.org/10.2514/1.39211.

[17] J. Slough, High beta plasma for inflation of a dipolar magnetic field as a magnetic sail, in: Proceedings of the IEPC Conference, Citeseer, 2001, pp. 14–19.

[18] J. Gunn, S. Carpentier-Chouchana, F. Escourbiac, T. Hirai, S. Panayotis, R. Pitts, Y. Corre, R. Dejarnac, M. Firdaouss, M. Kočan, et al., Surface heat loads on the ITER divertor vertical targets, Nucl. Fusion 57 (4) (2017) 046025, http://dx.doi.org/10.1088/1741-4326.

[19] I.A. Crawford, Project Icarus: A review of local interstellar medium properties of relevance for space missions to the nearest stars, Acta Astronaut. 68 (7–8) (2011) 691–699, http://dx.doi.org/10.1016/j.actaastro.2010.10.016.

[20] J.P. Kleijnen, Kriging metamodeling in simulation: A review, European J. Oper. Res. 192 (3) (2009) 707–716, http://dx.doi.org/10.1016/j.ejor.2007.10.013.

[21] W.E. Wiesel, Modern astrodynamics, Createspace, 2010.

[22] D. McComas, H. Elliott, N. Schwadron, J. Gosling, R. Skoug, B. Goldstein, The three-dimensional solar wind around solar maximum, Geophys. Res. Lett. 30 (10) (2003) http://dx.doi.org/10.1029/2003GL017136.

[23] Y. Guo, R.W. Farquhar, New Horizons mission design, Space Sci. Rev. 140 (1–4) (2008) 49–74, http://dx.doi.org/10.1007/s11214-007-9242-y.

[24] M. Leroux, K.J. Kihlstrom, S. Holleis, M.W. Rupich, S. Sathyamurthy, S. Fleshler, H. Sheng, D.J. Miller, S. Eley, L. Civale, et al., Rapid doubling of the critical current of YBa2Cu3O7- δ coated conductors for viable high-speed industrial processing, Appl. Phys. Lett. 107 (19) (2015) 192601, http://dx.doi.org/10.1063/1.4935335.

[25] P. Chaddah, Critical current densities in superconducting materials, Sadhana 28 (1–2) (2003) 273–282, http://dx.doi.org/10.1007/BF02717137.

[26] M. Raible, Concept Development for a Magnetic Sail Deceleration System (thesis), Technical University of Munich, 2013.

[27] A.R. Martin, Project Daedalus: The Final Report on the BIS Starship Study, British Interplanetary Society, 1978.

[28] A.M. Hein, N. Perakis, T.M. Eubanks, A. Hibberd, A. Crowl, K. Hayward, R.G. Kennedy III, R. Osborne, Project Lyra: Sending a spacecraft to 1I/'Oumuamua (former A/2017 U1), the interstellar asteroid, Acta Astronaut. 161 (2019) 552–561, http://dx.doi.org/10.1016/j.actaastro.2018.12.042.

[29] A. Hibberd, N. Perakis, A.M. Hein, Sending a spacecraft to interstellar Comet C/2019 Q4 (Borisov), 2019, arXiv preprint arXiv:1909.06348.

[30] A. Ruggiero, P. Pergola, S. Marcuccio, M. Andrenucci, Low-thrust maneuvers for the efficient correction of orbital elements, in: 32nd International Electric Propulsion Conference, 2011, pp. 11–15.